Oscillating Flexible Wings at Low Reynolds Numbers

D.J. Cleaver*, Z. Wang*, and I. Gursul†,
University of Bath, Bath, BA2 7AY, United Kingdom

In nature a range of techniques are used to overcome the challenges of low Reynolds number flight. In this paper two of these are considered, wing oscillations and wing flexibility. The force, deformation and flow fields of rigid and flexible wings oscillating at a fixed post-stall angle of attack of 15° and amplitude of 15% of chord are measured. The force measurements show that flexibility can increase the time-averaged lift coefficient significantly, oscillation at a Strouhal number of Sr_c = 1.5 results in C_l = 2.43 for the flexible wing as opposed to C_l = 1.13 for the rigid wing. Simultaneously, flexibility reduces the power input coefficient, oscillation at / around the natural frequency of Sr_c = 1.5 results in a power coefficient of C_p = 2.4 for the flexible wing as opposed to C_p = 23.2 for the rigid wing. Deformation measurements show this frequency is associated with the tip motion lagging the root motion by 90° but with an amplitude 1.84 times greater. The velocity measurements show this deformation inhibits Leading-Edge Vortex (LEV) dipole formation resulting in a stronger LEV that convects closer to the upper surface. This combined with the stronger tip vortex explains the higher lift observed for the flexible wing.

Nomenclature

a	=	amplitude
c	=	chord length
C_D	=	time-averaged drag coefficient, $\overline{F_x}/0.5\rho csU_\infty^2$
C_L	=	time-averaged lift coefficient, $\overline{F_y}/0.5\rho csU_\infty^2$
C_P	=	time-averaged power coefficient, $\overline{F_y U_{pl}}/0.5\rho csU_\infty^3$
f	=	forcing frequency
F_x	=	instantaneous streamwise force
F_y	=	instantaneous cross-stream force
Re	=	Reynolds number
s	=	wing span
sAR	=	semi aspect ratio
Sr_A	=	Strouhal number based on amplitude, $2fa/U_\infty$
Sr_c	=	Strouhal number based on chord length, fc/U_∞
U_{pl}	=	instantaneous plunging velocity
U_∞	=	freestream velocity
u	=	streamwise velocity
v	=	cross-stream velocity
w	=	spanwise velocity
x	=	streamwise direction
y	=	cross-stream direction
z	=	spanwise direction
α	=	angle of attack
λ	=	elastic parameter, $EI/0.5\rho U_\infty^2 s^3$
θ	=	phase lag relative to root
ω	=	vorticity magnitude
ω_z	=	spanwise vorticity

* Lecturer, Department of Mechanical Engineering, Member AIAA.
† Professor, Department of Mechanical Engineering, Associate Fellow AIAA.

I. Introduction

For decades the research community has been fascinated by natural flight both in its own right, and also as an example of the type of performance desirable for Micro Air Vehicles (MAVs). The truly exceptional performance of birds and insects, in terms of speed and agility, often exceeds man made aircraft on a like-for-like basis [1]. During the latter part of the 20th century it became clear that this exceptional performance is far greater than that achievable under steady or quasi-steady conditions. It is therefore reasonable to suppose that natural flyers employ unsteady mechanisms to overcome the challenges of low Reynolds number flight. Of the unsteady aerodynamic phenomenon the Leading Edge Vortex (LEV) is generally accepted [2,3] as being responsible for creating the majority of the large time-averaged lift forces, making it crucial for low Reynolds number flapping flight. It has been shown [4] that similar LEVs and high time-averaged lift coefficients can be created by small-amplitude high-frequency motion, which could be more appropriate for electrical actuators. The maximum time-averaged lift coefficient observed was 305% larger than that achieved under steady-state conditions and was accompanied by thrust.

A further aspect of natural flight is the aeroelastic interaction of the lightweight structure with the large inertial and aerodynamic forces which invariably leads to deformation [5,6]. There is a small but growing body of evidence that this passive deformation can improve lift and thrust generation although the exact detail and mechanisms remain unresolved [5]. Several studies for chordwise [7,8] and spanwise [8-10] flexible wings have shown that optimal flexibility, and therefore deformation, can improve thrust performance in terms of both time-averaged thrust coefficient and propulsive efficiency. For the chordwise flexible cases, the thrust was improved through stronger trailing-edge vortices spaced further apart leading to a stronger time-averaged jet. For spanwise flexible wings, operating at $Sr_A > 0.2$, appropriate flexibility was found to simultaneously increase thrust coefficient slightly and reduce power coefficient slightly resulting in an increase in efficiency. Chimakurthi et al. [10] postulated that the increased thrust was a result of higher local instantaneous effective angles of attack, promoting larger streamline curvatures and thus greater leading-edge suction. The effect of flexibility on time-averaged lift was not considered.

The main objective of this paper is to study the effect of flexibility on lift performance in the post-stall regime. Force, deformation, two-dimensional particle image velocimetry and three-dimensional defocused digital particle image velocimetry (here termed volumetric velocimetry) measurements are presented for rigid and flexible flat plate wings oscillating with small-amplitude (a/c = 0.15) and range of Strouhal number ($Sr_c \leq 2.025$). These measurements will fully characterize the relation between force, deformation and flow field.

II. Experimental Apparatus and Procedures

Force, Digital Image Correlation (DIC), two-dimensional Particle Image Velocimetry (PIV) and volumetric velocimetry measurements were conducted for plunging rigid and flexible wings mounted vertically in a closed-loop water tunnel, see Fig. 1a. For a review of parameters studied, see Table 1; uncertainties are calculated based on the methods of Moffat [11] taking into account both bias and precision errors.

Table 1 Experimental Parameters

Parameter	Range Considered	Uncertainty
Re	10,000	+/- 200
α	15°	+/- 0.5°
a/c	0.15	+/- 0.003
Sr_c	0 to 2.025	+/- 2.3%

A. Experimental Setup

The experiments were conducted in a free-surface closed-loop water tunnel (Eidetics Model 1520) at the University of Bath. The water tunnel is capable of flow speeds in the range 0 to 0.5 m/s and has a working section of dimensions 381 mm x 508 mm x 1530 mm. The turbulence intensity has previously [12] been measured by LDV to be less than 0.5%.

Mounted on top of the tunnel is the experimental rig, see Fig. 1a. The oscillations were supplied via a Motavario 0.37 kW three-phase motor, 5:1 wormgear and IMO Jaguar Controller. The position of the root of the airfoil was measured through a rotary encoder attached to the spindle of the worm gear shaft. The rotary encoder was also used to trigger the DIC, PIV and volumetric velocimetry systems.

In this report three wings are considered: a rigid flat plate (RFP), a flexible plate (FP) and a highly flexible plate (HFP). The RFP wing was fabricated from mild steel of thickness 0.04c. The FP and HFP wings were of thickness 0.03c and fabricated from acrylic and polyethylene respectively. The flexible material was held in a mild steel holder to guarantee chordwise rigidity along the root, see Fig. 2. The deformation is therefore predominantly spanwise bending. All wings have semi-circular leading and trailing edges and dimensions of 0.1 m chord and 0.3 m span. The rigidity of the highly flexible wing was measured as: $\lambda = 21.1$; the rigid wing can be taken as: $\lambda = 639.7$.

B. Force Measurements

The force in the streamwise direction was measured through a two-component binocular strain gauge force balance [13]. Two force balances of differing rigidities were used so as to achieve the desired accuracy whilst minimizing flexibility. The signal from the strain gauges was amplified by a Wheatstone bridge circuit and sampled at either 1 kHz for 20,000 samples (stationary cases), or 360 per cycle (dynamic cases). The forces were then calculated from the average voltage through linear calibration curves. The calibration curves consisted of twenty three points, and were performed daily before and after testing. Each data set consists of an average of at least four individual runs.

C. Digital Image Correlation Measurements

The deformation of the highly flexible wing was measured with a Limess DIC system. This consists of a pair of Photron SA3 cameras, which are capable of image acquisition with a resolution of 1024 x 1024 pixels at 1,000 fps, with the images processed in VIC-3D. Normally these cameras are mounted at an angle to each other to give depth information and the same field of view. In the current scenario this was not appropriate because refraction at the water-glass-air interface leads to image warping which will give erroneous results. To minimise this effect the cameras were instead kept parallel and the angle was created by angling the lenses with Scheimpflug mounts, see Fig. 1b. The measurements were validated before each measurement by measuring the stationary rigid wing as it is manually moved through 5 mm steps in the range: 0 to 30 mm. The error was always less than 0.15% of the chord length. The calibration consisted of at least 60 images of a randomly orientated 12 x 9 grid. The majority of results shown herein are instantaneous results for Strouhal numbers of $Sr_c = 0.075$ to 2.025 with a $Sr_c = 0.075$ interval. These were acquired at a rate of twenty four images per cycle for a minimum of ten cycles. The midchord position, deformation, twist angle, effective angle of attack, amplitude, and phase along the span were then derived in MATLAB by taking 1 mm wide slices at regular spanwise locations. The wings shown in the PIV and velocimetry figures were built from the phase-averaged deformation measurements.

D. 2D PIV Measurements

The flow was seeded with 8 – 12 μm hollow glass spheres. The velocity field around the airfoil was measured using a TSI Inc. 2D-PIV system incorporating a dual ND:YAG 50 mJ pulsed laser, 2 MP Powerview Plus 12 bit CCD camera and TSI Model 610034 synchronizer. For the measurements over the upper surface the laser was positioned behind with the camera below, see Fig. 3a. The shadow created by the airfoil therefore obscured the lower surface. For measurements over the lower surface the laser was rotated 90 degrees, see Fig. 3b. The PIV images were analyzed using the software Insight 3G using an FFT correlator with interrogation windows of 32 x 32 pixels to generate a vector field of 99 x 73 vectors, approximately giving a 2 mm spatial resolution. Upper and lower surface measurements were performed at $z/s = 0.05$ intervals from $z/s = 0.05$ to 1.20, to give 24 individual planes.

E. Volumetric Velocimetry Measurements

The volumetric flow measurements were acquired using a three-component velocimetry (TSI V3V™) system based on the techniques developed by Pereira et al. [14] for defocusing digital particle image velocimetry (DDPIV). The flow was seeded with 50 μm hollow glass particles. The volume of interest was illuminated using a dual ND:YAG 200 mJ pulsed laser, equipped with two cylindrical lenses offset by 90 degrees from each other to generate a laser cone, see Fig. 4. The laser cones were fired 700 μs apart. The images were acquired using three 4MP 12 bit CCD cameras placed to form an equilateral triangle whose common focal plane defines the most distant plane within the volume of interest. DDPIV uses multiple off-axis apertures to generate multiple defocused particle images where the particle's separation distance and location give its position in three-dimensional space. If the three images of a single particle were superimposed, the particle would appear as a triangle with its centre equating to its x-y coordinates and the size of the triangle equating to its z coordinate. The cameras were calibrated by translating a rectangular plate of regularly spaced grid dots across the volume of interest with image triplets acquired at 5 mm intervals to generate a camera signature graph.

There are four stages from image to gridded velocity data. First the particles are identified in each of the 6 captured images (two times of three), using a 2D particle identification algorithm. Second, the particles are grouped between the three images to form complete triplets. Using the triangles generated during the calibration stage this gives two sets of three-dimensional particle coordinates equating to the two times. Third, the particles are 'tracked' through a 3D particle tracking algorithm using the relaxation method first proposed by Baek and Lee [15]. This essentially uses an iterative process to update the probability of two particles matching between two frames, at each step, using neighbour particle displacement similarity criteria as well as flow estimates, and then choosing the particle match with greatest probability. This is outlined in more detail by Pereira et al. [16]. A median filter was applied to remove any outliers. Finally the randomly spaced vectors from 200 separate phase-locked measurements are interpolated onto a uniformly spaced grid of voxel size 8 mm with a 55% overlap to give phase-averaged uniformly spaced velocity vectors. The grid interpolation produced 25,000 to 37,000 grid vectors within a measurement volume of 140 × 140 × 90 mm.

To capture the entire span, it was necessary to perform measurements separately for five volumes from $z/s = 0$ to 1.2. Unfortunately, the upper surface of the airfoil was largely obscured in several phases by the wing itself, see Fig. 5. This effect was particularly severe for the HFP wing due to the larger deformation. It was not possible to angle the cameras due to the image warping that would be created by the water-glass-air interface, and a water prism was not practical due to the obstruction created by the water tunnel's structural supporting bars (see Fig. 4). Instead to capture data within the obscured region measurements were performed using 2D-PIV with the camera tilted six degrees to the horizontal. This angle will create image warping so that measurements will differ across the area of interest. To quantify this error, time-averaged measurements were performed for the same area in the centre of the tunnel, with no model, with and without an angle applied. The difference between the two sets of measurements is less than 1% of the freestream velocity, see Fig. 6. Shown in Fig. 7 is a comparison of results acquired using 2D-PIV and volumetric velocimetry for the highly flexible wing at a single phase in the cycle ($t/T = 0.75$). Generally the results match quantitatively very well. Both show a leading-edge vortex that is stronger at the root, and a separated trailing-edge vortex of opposite sign with a kinked region near the tip. Both sets of measurements also show a small region of negative vorticity over the airfoil's surface around $z/s = 2/3$. In Fig. 7 spanwise vorticity (ω_z) is used because 2D-PIV only acquires the u and v components of velocity so it is not possible to derive chordwise, cross-stream, or vorticity magnitude. The question therefore arises is it appropriate to use only spanwise vorticity in the obscured region? In answer, shown in Fig. 8 is an isosurface of $\omega c/U_\infty = 25$ overlaid with contours of ω_z/ω acquired using DDPIV. Where the isosurface is dark red or blue, over 95% of the vorticity is spanwise. In the region $z/s = 0$ to 0.9 the flow is therefore predominantly two-dimensional and it is appropriate to use 2D-PIV measurements. The u and v components of velocity from the 2D-PIV measurements were therefore used to fill in the obscured region in the volumetric data in the region $z/s = 0$ to 0.9, with only DDPIV data used outside of this region.

The five volumes of DDPIV and twenty-four slices of 2D-PIV data were combined in MATLAB through interpolation onto a common grid. The desired flow properties such as vorticity magnitude are then calculated. These flow properties were then imported into Tecplot 360™ for plotting, along with a model of the wing built from the phase-averaged DIC measurements.

III. Results and Discussion

A. Force Measurements

Shown in Fig. 9 are time-averaged lift, drag and power coefficient for the rigid, flexible, and highly flexible wings oscillating with an amplitude of $a/c = 0.15$ and $\alpha = 15°$. Also shown are force measurements for a 'two-dimensional' rigid wing (2D Rigid, open triangles and dashed lines). This wing is identical to the rigid wing except with a lower end plate added at the tip. The results for this wing have previously been presented [17]. The salient features are a general increase in lift coefficient to give an almost linear trend with Sr_A due to growing strength of the upper surface leading-edge vortex. Superimposed onto this linear trend are several peaks due to resonance at the natural shedding frequency, its harmonics, and subharmonics. At higher Strouhal numbers there is a gradual reduction in lift coefficient due to the upper surface and lower surface LEVs forming a dipole that convects upwards resulting in increased time-averaged separation. This increased time-averaged separation is also reflected in the drag coefficient where at the maximum Strouhal numbers there is a negligible reduction in drag coefficient. This is in stark contrast to the very large thrust coefficients ($C_d = -2.76$) observed for a NACA 0012 airfoil oscillating at identical conditions.

The effect of the tip vortex is demonstrated through comparison of the 2D Rigid and 3D Rigid (closed triangles, solid lines) cases. Time-averaged lift coefficient for the 3D Rigid wing demonstrates the same qualitative trends as the 2D Rigid except with consistently lower values. Initially this difference is small, but tends to grow with increasing Strouhal number. As a result the maximum lift coefficient is significantly lower: C_l = 1.75 versus 2.59, an increase over the stationary case of 120% for the 3D case as opposed to 178% for the 2D. By contrast the time-averaged drag coefficient is consistently reduced by the three-dimensionality and the comparative improvement grows with increasing Strouhal number. This surprising reduction in drag coefficient when a tip vortex is present is most likely due to the angle of the total force relative to the wing remaining approximately constant. Hence, when the increase in lift is reduced, drag is also likely to be reduced. Consequently the lower lift for the rigid wing means that at the highest Strouhal number there is a very small thrust coefficient. Time-averaged power coefficient is also consistently reduced in the 3D case. There is the same parabolic trend as observed by Heathcote & Gursul [7] and Young and Lai [18] except with a steeper gradient for the 2D Rigid wing.

The effect of flexibility is demonstrated by comparison of the 3D Rigid with the 3D Flexible (solid squares, solid lines) and 3D Highly Flexible (solid circles, solid lines) curves. At low Strouhal numbers (Sr_c < 0.8) there is negligible effect on time-averaged lift coefficient. At higher Strouhal numbers (Sr_c > 0.8) the three curves diverge with increasing flexibility leading to significantly larger lift coefficients. For the highly flexible case the peak lift coefficient is C_l = 3.07, an increase of 278% over the stationary airfoil. Similarly at low Strouhal numbers there is negligible effect on time-averaged drag coefficient. At $Sr_c \approx 0.8$ the three curves diverge with greater flexibility leading to larger drag coefficient, reflecting the increasing lift coefficient in this range. The time-averaged power coefficient is strongly dependent on flexibility, for both the flexible and highly flexible cases there are inflection points. For the highly flexible cases this inflection leads to a minimum at $Sr_c \approx 1.5$. This value closely matches the wing's natural frequency, measured by applying an impulsive motion to the wing in stationary water and then measuring the oscillations in lift. Furthermore for the flexible wing there is the suggestion of a similar minimum around the natural frequency of $Sr_c \approx 2.2$, however this is outside the measured range and so cannot be confirmed. These power coefficient measurements are however calculated using solely the instantaneous cross-stream force and cross-stream velocity and therefore do not include the contribution due to moment. In the future these measurements will be validated through direct measurement of the electrical power.

B. Deformation Measurements

Deformation measurements were performed across the entire Strouhal number range for all three wings however for conciseness only the results for the highly flexible wing shall be considered here. Shown in Fig. 10 are the midchord positions along the span of the wing for four representative Strouhal numbers at twelve selected instants. Solid lines represent when the root is moving downwards; dashed lines represent when the root is moving upwards. At Sr_c = 0.075 there is an almost linear deformation along the span. Due to the low frequency the inertia force is minimal and the deformation is the same regardless of whether the root is moving up or down. With the frequency increased to Sr_c = 0.975 the inertia force is greater and there is therefore a difference between the up and down instants. When moving down the wing tends to be deformed upwards, and when moving up the wing tends to be deformed downwards. This indicates that the tip motion lags behind the root motion. In addition, the amplitude of this tip motion is larger than the root amplitude. Increasing the Strouhal number to Sr_c = 1.500 results in further increase in tip amplitude. In addition, the deformation is greater resulting in a larger phase lag between the root and tip. Increasing the Strouhal number again to the maximum studied: Sr_c = 2.025, the deformation increases again however the tip amplitude is clearly reduced. As will be demonstrated later this reduction in tip amplitude is due to the phase lag becoming greater than θ = 90°.

Shown in Fig. 11 are measurements of the variation of amplitude and phase lag along the span of the wing for all of the 27 Strouhal numbers tested. At low Strouhal numbers, amplitude shows a parabolic trend with steeper gradient for greater Strouhal number. The tip amplitude therefore increases with increasing Strouhal number. After Sr_c = 1.125 the initial gradient at z/s = 0 begins to reduce with increasing Strouhal number. Despite this decrease in initial gradient the gradient becomes steeper again further along the span. Thus, the tip amplitude continues to increase in this regime. At Sr_c = 1.350 the decrease in initial gradient results in a negative initial gradient. There is therefore an inflexion point at $z/s \approx 0.3$. This Strouhal number corresponds to the peak tip amplitude. Further increase beyond this Strouhal number is represented by a dashed line and results in a greater negative initial gradient, a smaller minimum, and reducing tip amplitude. Phase lag consistently increases along the span with an inflexion point at $z/s \approx 0.5$. The phase lag also consistently increases with Strouhal number.

Shown in Fig. 12 is the tip amplitude ratio (solid line) and tip phase lag (dashed line) against Strouhal number. Initially the amplitude ratio consistently increases reaching a maximum at $Sr_c = 1.350$ of $a_{tip}/a_{root} = 1.93$, and then decaying after. The tip phase lag consistently increases. For this wing the natural frequency was measured as $Sr_c \approx 1.5$. This is slightly above the peak tip amplitude however one would expect this behaviour in a system with damping. The tip phase-lag for this Strouhal number is $\varphi = 90°$. A three-dimensional representation of the deformation for this Strouhal number is shown in Fig. 13. The symbols are the experimentally measured trailing-edge points with time; the lines are the sine fit curves to these points. Generally the agreement is excellent along the entire span. Due to the high lift experienced at $Sr_c = 1.500$ (see Fig. 9) for the highly flexible wing, and also because it is the wing's natural frequency, $Sr_c = 1.500$ was selected for velocity measurements.

C. Velocity Measurements

Shown in Fig. 14 are isosurfaces of phase-averaged vorticity magnitude overlaid with contours of spanwise vorticity for the rigid wing at twelve phases in the cycle. The phases are in a counter-clockwise loop starting with the top of the motion ($t/T = 0/12$) moving down through the left column to the bottom of the motion ($t/T = 6/12$) before moving back up through the right column to reset the motion to the top. For the rigid wing, the root and tip move in-phase. Starting with the top of the motion ($t/T = 0/12$), behind the trailing-edge there is a region of clockwise vorticity. This is the remnants of a TEV formed during the upward motion which has now convected outside the measurement volume. Above the leading-edge there are weak regions of clockwise vorticity a large distance above the leading-edge. This appears to be the remnants of a clockwise upper-surface LEV. Once the wing begins moving downwards ($t/T = 0/12$ to $3/12$) this vague LEV appears to remain stationary over the upper surface. The phase $t/T = 3/12$ is the point of peak downwards velocity, as such there is a strong counter-clockwise TEV and tip vortex. With further progression downwards ($t/T = 3/12$ to $6/12$) these continue to grow reaching their maximum strength at $t/T = 6/12$. The vague region of vorticity over the leading-edge still remains stationary and relatively unchanged. For a two-dimensional flat plate airfoil operating at the same conditions (Cleaver *et al.* [17]) one would expect a LEV dipole. This is where the upper surface clockwise vortex forms a dipole with the counter-clockwise lower surface LEV. This dipole convects in an upstream direction resulting in the rapid dissipation of both vortices to leave a 'plume' of vorticity. Similar behaviour has also been observed for finite wings [19]. In this case, the experimental conditions were slightly different: $\alpha = 20°$ instead of 15°, $Re = 20{,}000$ instead of 10,000, and $Sr_c = 1.350$ instead of 1.500. Nevertheless a LEV dipole is still present for $sAR = 2$, but is not visible because the velocity measurements start at the leading-edge. Instead only the remnants of the dipole are visible. With the wing moving upwards ($t/T = 6/12$ to $0/12$) the counter-clockwise TEV and tip vortex convect downstream and a new clockwise TEV forms (partially obscured by the convecting counter-clockwise TEV).

Shown in Fig. 15 are the volumetric velocimetry measurements for the highly flexible wing. Due to the generally larger vorticity levels in this case it was necessary to raise the minimum isosurface level to $\omega c/U_\infty = 12$ from 8. In this case the deformation of the wing means the motion of the wing is more complicated. Due to the phase lag of $\theta = 90°$ the tip lags behind the root wing by $t/T = 3/12$. Therefore, at $t/T = 0/12$ the root has reached the top of the motion and has zero vertical velocity, whereas the tip is passing through the centre of its motions and has maximum vertical velocity. In this phase, there is again a clear TEV, tip vortex, and a much stronger region of clockwise vorticity over the upper surface indicative of an LEV. The strength of all three is greater than that observed for the rigid wing. As the root moves downwards ($t/T = 0/12$ to $3/12$) the tip moves upwards strengthening the lower surface tip vortex. The LEV convects downstream dissipating as it progresses. At $t/T = 3/12$ the root is moving downwards with maximum velocity whilst the tip has reached the top of its motion. The lower surface tip vortex can be observed below the tip, and an upper surface tip vortex is beginning to form. As the tip begins to move downwards ($t/T = 3/12$ to $6/12$) this upper surface tip vortex grows in strength, and one also begins to observe a new upper surface LEV and TEV. As the root moves upwards ($t/T = 6/12$ to $9/12$) the tip continues to move downwards reaching the bottom of its motion at $t/T = 9/12$. There is a strong counter-clockwise TEV formed during the downward motion which is shed first from the root and later from the tip. There is a very complex tip vortex similar to those described in Calderon *et al.* [19], and a relatively strong clockwise LEV. For all three vortices the maximum levels of vorticity are significantly higher than those observed for the rigid wing, especially taking into account the higher isosurface levels in Fig. 15. The significantly higher lift can therefore be attributed to the flexibility inhibiting LEV dipole formation, resulting in a stronger upper surface LEV that convects closer to the upper surface, and a stronger tip vortex [20].

IV. Conclusions

Force, digital image correlation, two-dimensional PIV, and three-dimensional volumetric velocimetry measurements were performed for rigid and flexible finite wings undergoing small-amplitude plunge oscillations with a fixed post-stall angle of attack. Optimally flexible wings were shown to significantly increase lift, C_l = 2.43 for the flexible wing as opposed to C_l = 1.13 for the rigid wing at Sr_c = 1.5. Deformation measurements showed oscillation of the flexible wing at the natural frequency resulted in spanwise bending such that the tip lagged the root by 90° with an amplitude 1.84 times larger. Due to this large amplitude tip motion, a very large and complex tip vortex forms. In addition the three-dimensionality created by the deformation inhibits the formation of the LEV dipole observed for the rigid wing, to give a stronger LEV that convects closer to the upper surface of the wing. The combination of strong LEV and tip vortex results in significantly higher lift for significantly less power.

Acknowledgments

The work was supported by the Air Force Office of Scientific Research, Air Force Material Command, USAF under grant number FA8655-09-1-3007, the RCUK Academic Fellowship in Unmanned Air Vehicles, and the EPSRC loan pool.

References

[1]Shyy, W., Berg, M., and Ljungqvist, D., "Flapping and Flexible Wings for Biological and Micro Air Vehicles," *Progress in Aerospace Sciences*, Vol. 35, No. 5, 1999, pp. 455-505.

[2]Ho, S., Nassef, H., Pornsinsirirak, N., Tai, Y.C., and Ho, C.M., "Unsteady Aerodynamics and Flow Control for Flapping Wing Flyers," *Progress in Aerospace Sciences*, Vol. 39, No. 8, 2003, pp. 635-681.

[3]Sane, S.P., "The Aerodynamics of Insect Flight," *Journal of Experimental Biology*, Vol. 206, No. 23, 2003, pp. 4191-4208.

[4]Cleaver, D.J., Wang, Z., and Gursul, I., "Lift Enhancement by Means of Small Amplitude Airfoil Oscillations at Low Reynolds Numbers," *AIAA Journal*, Vol. 49, No. 9, 2011, pp. 2018 - 2033.

[5]Mountcastle, A.M., and Daniel, T.L., "Aerodynamic and Functional Consequences of Wing Compliance," *Experiments in Fluids*, Vol. 46, No. 5, 2009, pp. 873-882.

[6]Biewener, A.A., and Dial, K.P., "In-Vivo Strain in the Humerus of Pigeons (Columba-Livia) During Flight," *Journal of Morphology*, Vol. 225, No. 1, 1995, pp. 61-75.

[7]Heathcote, S., and Gursul, I., "Flexible Flapping Airfoil Propulsion at Low Reynolds Numbers," *AIAA Journal*, Vol. 45, No. 5, 2007, pp. 1066-1079.

[8]Shyy, W., Aono, H., Chimakurthi, S.K., Trizila, P., Kang, C.K., Cesnik, C.E.S., et al., "Recent Progress in Flapping Wing Aerodynamics and Aeroelasticity," *Progress in Aerospace Sciences*, Vol. 46, No. 7, 2010, pp. 284-327.

[9]Heathcote, S., Wang, Z., and Gursul, I., "Effect of Spanwise Flexibility on Flapping Wing Propulsion," *Journal of Fluids and Structures*, Vol. 24, No. 2, 2008, pp. 183-199.

[10]Chimakurthi, S.K., Tang, J., Palacios, R., Cesnik, C.E.S., and Shyy, W., "Computational Aeroelasticity Framework for Analyzing Flapping Wing Micro Air Vehicles," *AIAA Journal*, Vol. 47, No. 8, 2009, pp. 1865-1878.

[11]Moffat, R.J., "Describing the Uncertainties in Experimental Results," *Experimental Thermal and Fluid Science*, Vol. 1, No. 1, 1988, pp. 3-17.

[12]Heathcote, S. "Flexible Flapping Airfoil Propulsion at Low Reynolds Numbers," Ph.D. Dissertation, Dept of Mechanical Engineering, University of Bath, Bath, 2006.

[13]Frampton, K.D., Goldfarb, M., Monopoli, D., and Cveticanin, D. "Passive Aeroelastic Tailoring for Optimal Flapping Wings". *Fixed and Flapping Wing Aerodynamics for Micro Air Vehicle Applications* Amer Inst Aeronautics & Astronautics, Reston, 2002, pp. 473-482.

[14]Pereira, F., and Gharib, M., "Defocusing Digital Particle Image Velocimetry and the Three-Dimensional Characterization of Two-Phase Flows," *Measurement Science & Technology*, Vol. 13, No. 5, 2002, pp. 683-694.

[15]Baek, S.J., and Lee, S.J., "A New Two-Frame Particle Tracking Algorithm Using Match Probability," *Experiments in Fluids*, Vol. 22, No. 1, 1996, pp. 23-32.

[16]Pereira, F., Stuer, H., Graff, E.C., and Gharib, M., "Two-Frame 3d Particle Tracking," *Measurement Science & Technology*, Vol. 17, No. 7, 2006, pp. 1680-1692.

[17]Cleaver, D.J., Wang, Z., and Gursul, I., "Investigation of Mechanisms of High Lift for a Flat-Plate Airfoil Undergoing Small-Amplitude Plunging Oscillations," *AIAA Journal*, in press, 2012.

[18]Young, J., and Lai, J.C.S., "Mechanisms Influencing the Efficiency of Oscillating Airfoil Propulsion," *AIAA Journal*, Vol. 45, No. 7, 2007, pp. 1695-1702.

[19]Calderon, D.E., Wang, Z., and Gursul, I. "Volumetric Measurements and Simulations of the Vortex Structures Generated by Low Aspect Ratio Plunging Wings " *50th AIAA Aerospace Sciences Meeting*, AIAA-2012-914, Nashville, Tennessee, 2012.
[20]Shyy, W., Trizila, P., Kang, C.K., and Aono, H., "Can Tip Vortices Enhance Lift of a Flapping Wing?," *AIAA Journal*, Vol. 47, No. 2, 2009, pp. 289-293.

Figures

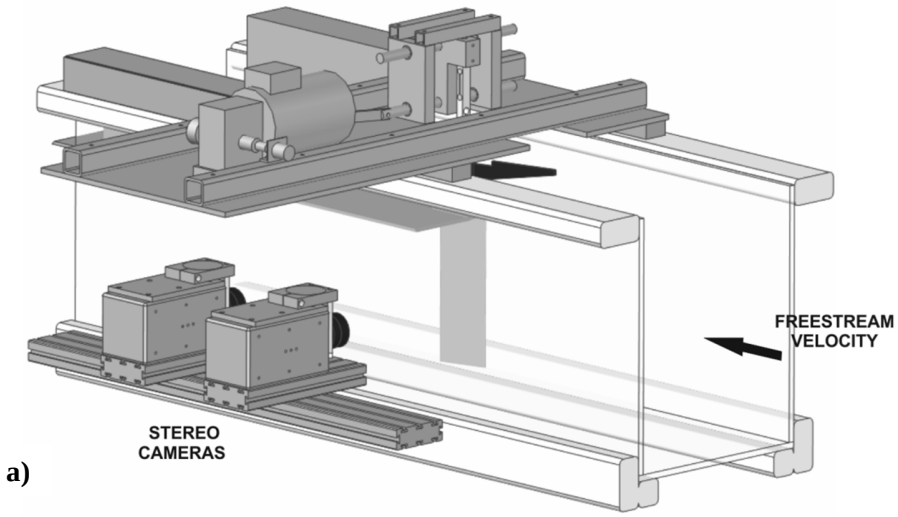

a)

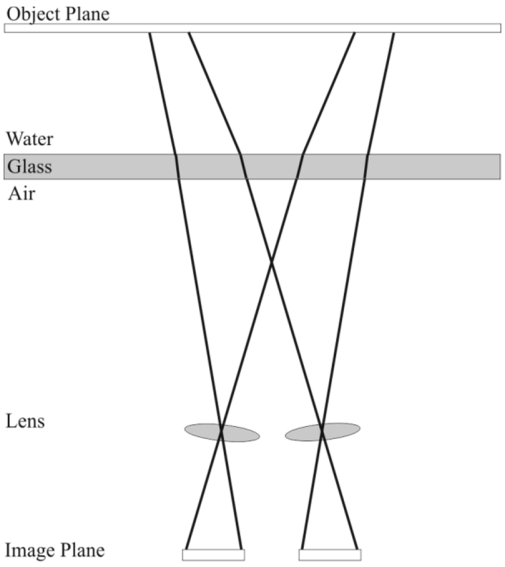

b)

Fig. 1 a) Digital image correlation setup, b) method used to correct for image warping using Scheimpflug mounts. Maximum error was always less than 0.15%*c*.

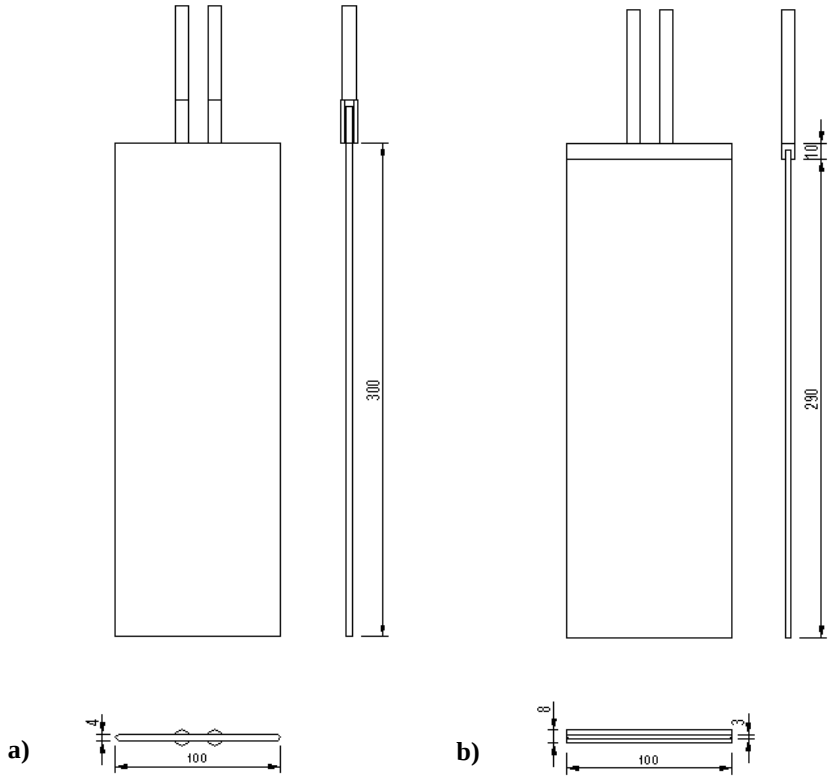

Fig. 2 Wing geometry: a) rigid wing, and b) flexible wings.

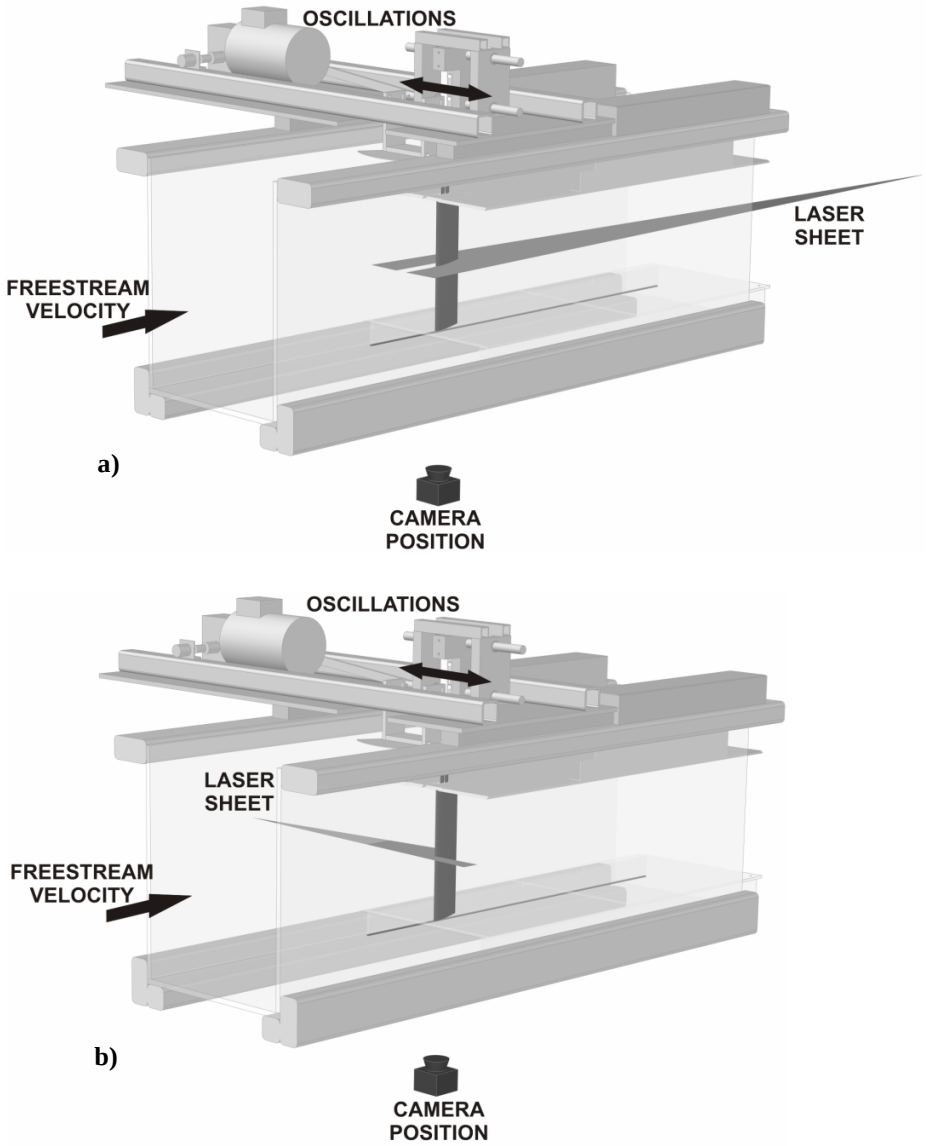

Fig. 3 2D-PIV experimental setup a) for measurements over the upper surface, and b) for measurements over the lower surface.

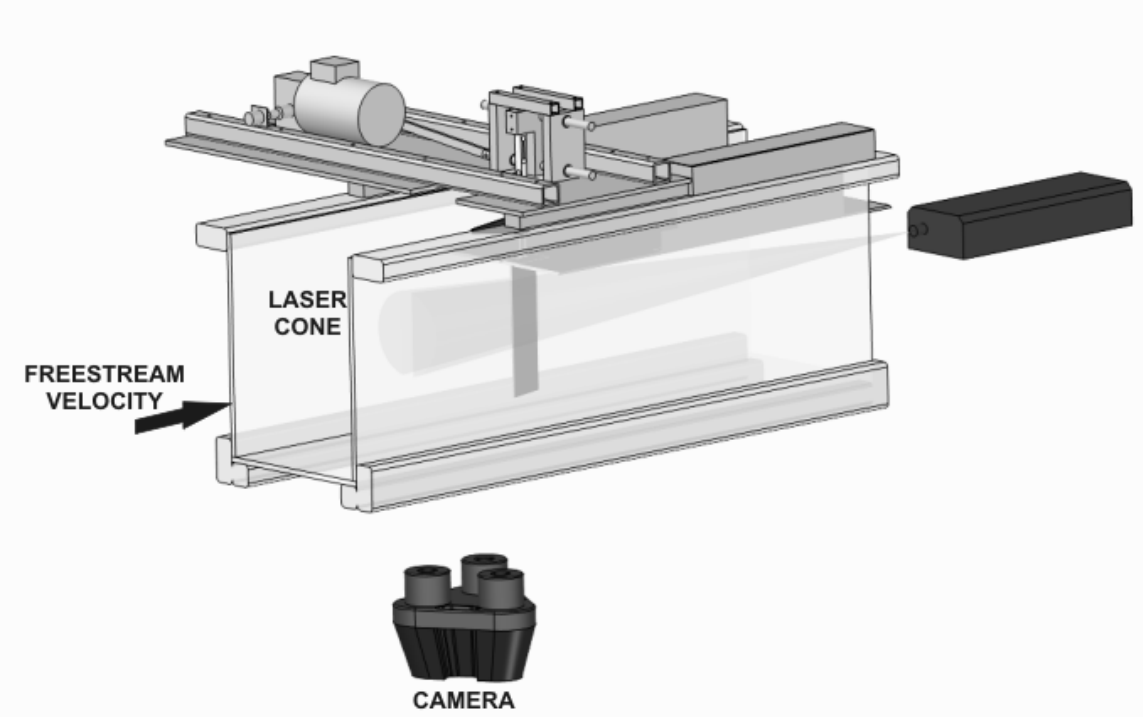

Fig. 4 Volumetric velocimetry experimental setup.

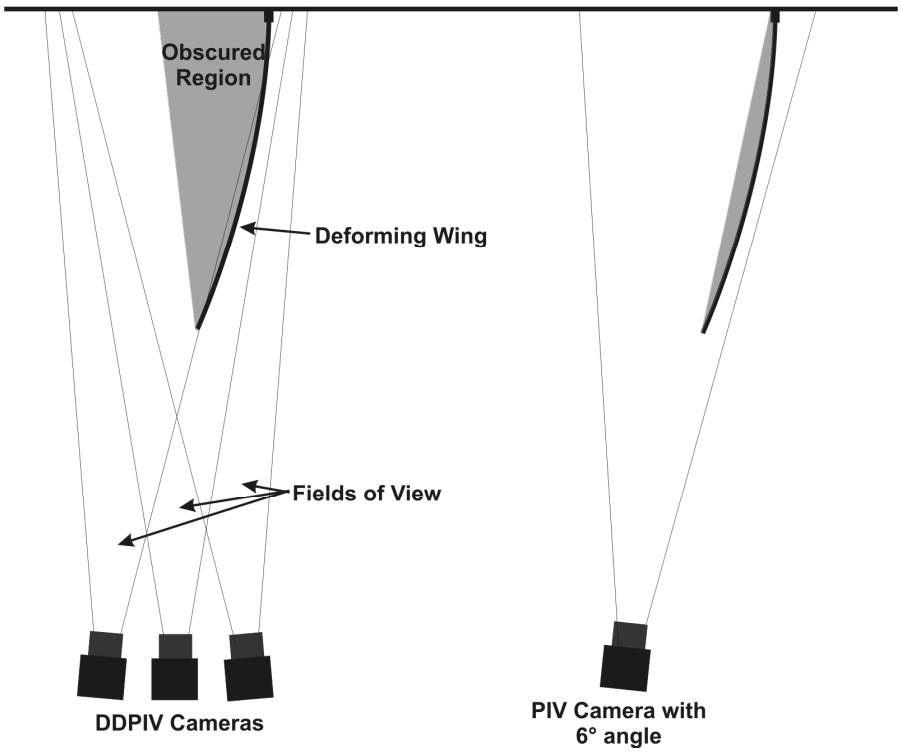

Fig. 5 Visual obstruction for DDPIV measurements (left) and comparison with 2D-PIV measurements (right).

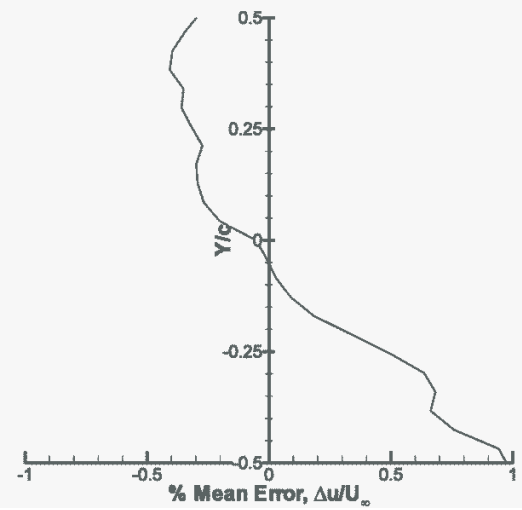

Fig. 6 Measured error due to the 6° 2D-PIV Camera tilt angle. Defined as the mean, along x, of the measured freestream velocity with 6° tilt angle subtracted from the measured freestream velocity with 0° angle.

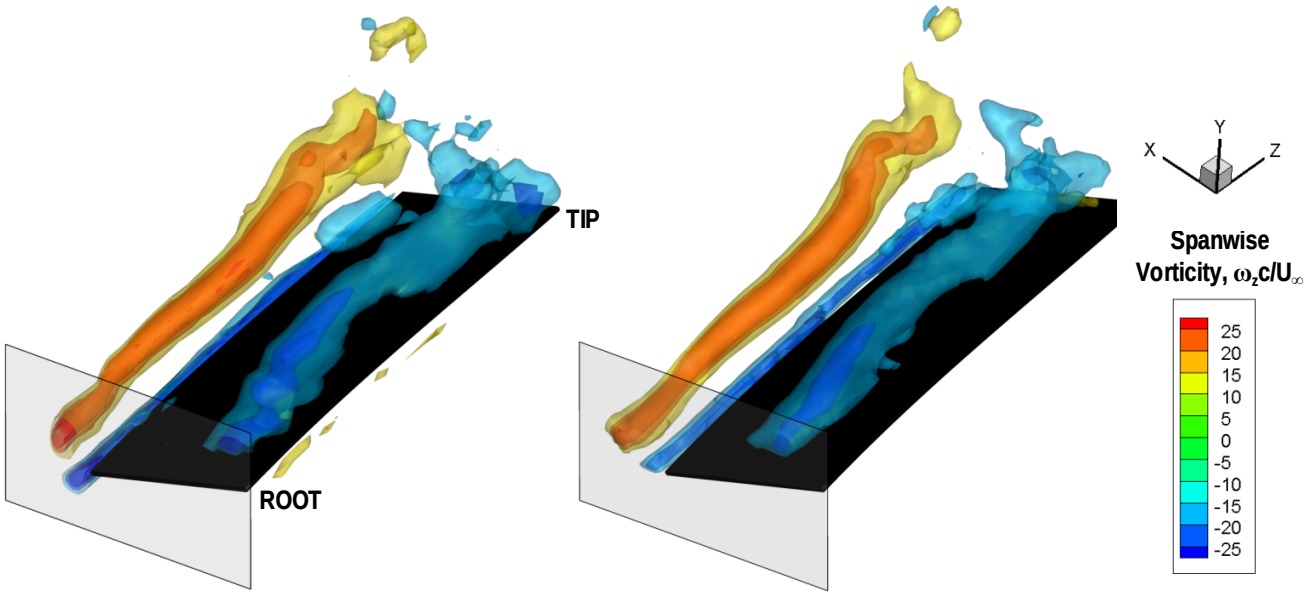

Fig. 7 Isosurfaces of phase-averaged (t/T = 0.75) spanwise vorticity ($\omega_z c/U_\infty$ = 15, 30, 45, -15, -30, and -45), acquired using 2D-PIV (left) and volumetric velocimetry (right) for the highly flexible wing oscillating with Sr_c = 1.500.

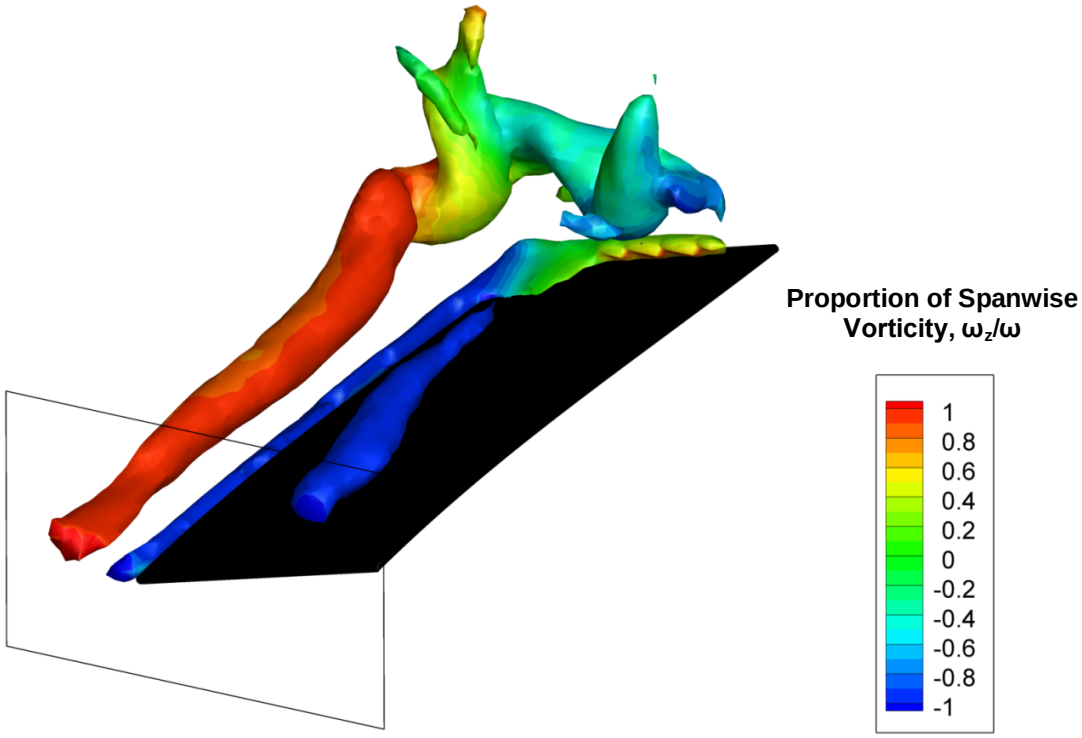

Fig. 8 A single isosurface of phase-averaged (t/T = 0.75) vorticity magnitude ($\omega c/U_\infty$ = 25) acquired using volumetric velocimetry for the highly flexible wing oscillating with Sr_c = 1.500. Where the isosurface is solid red or blue, spanwise vorticity is the primary contributor to vorticity magnitude.

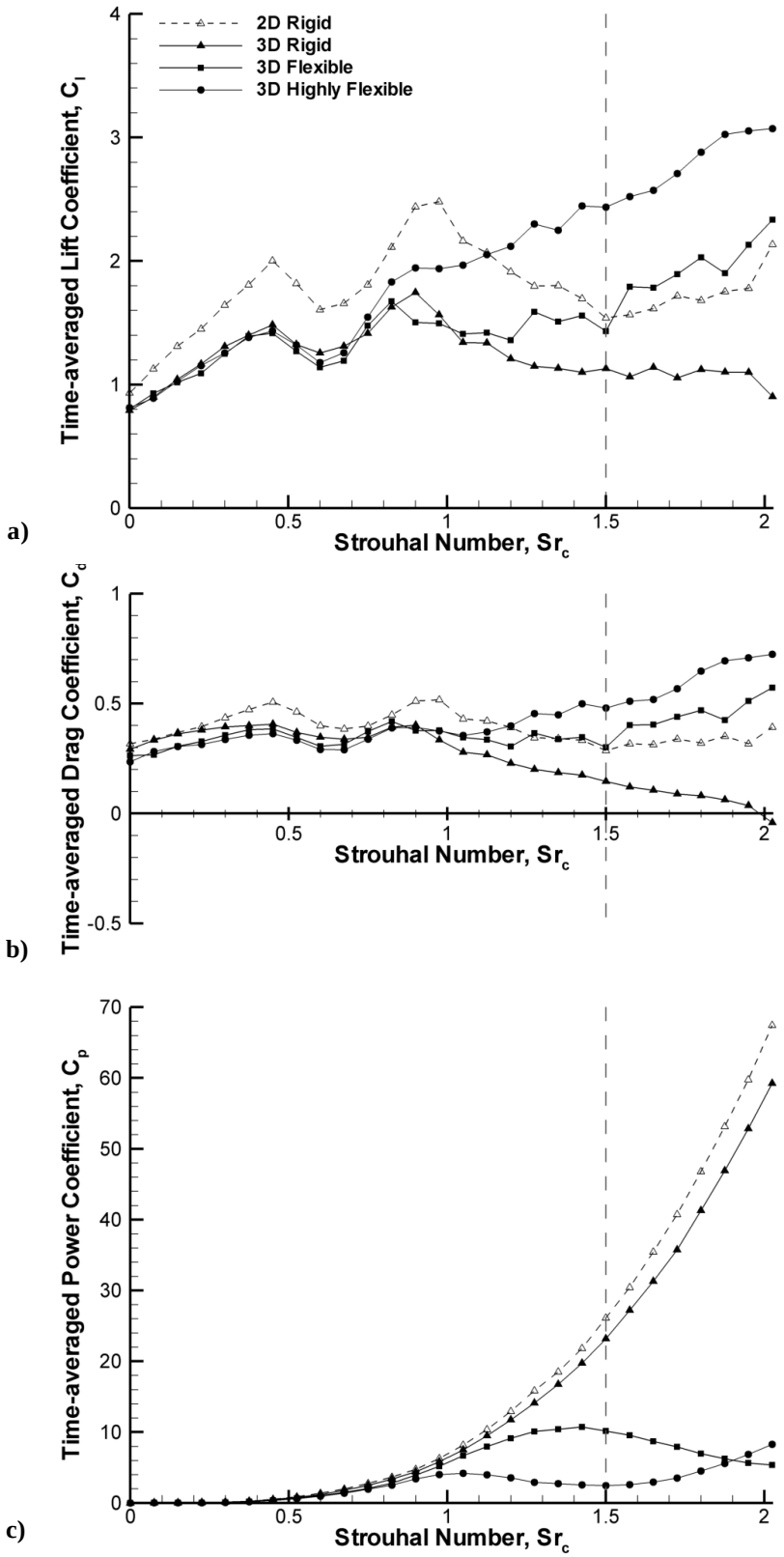

Fig. 9 Time-averaged a) lift coefficient, b) drag coefficient, and c) power coefficient for a/c = 0.150. The wing natural frequency was measured as $Sr_c \approx 2.2$ for the flexible wing and $Sr_c \approx 1.5$ for the highly flexible wing.

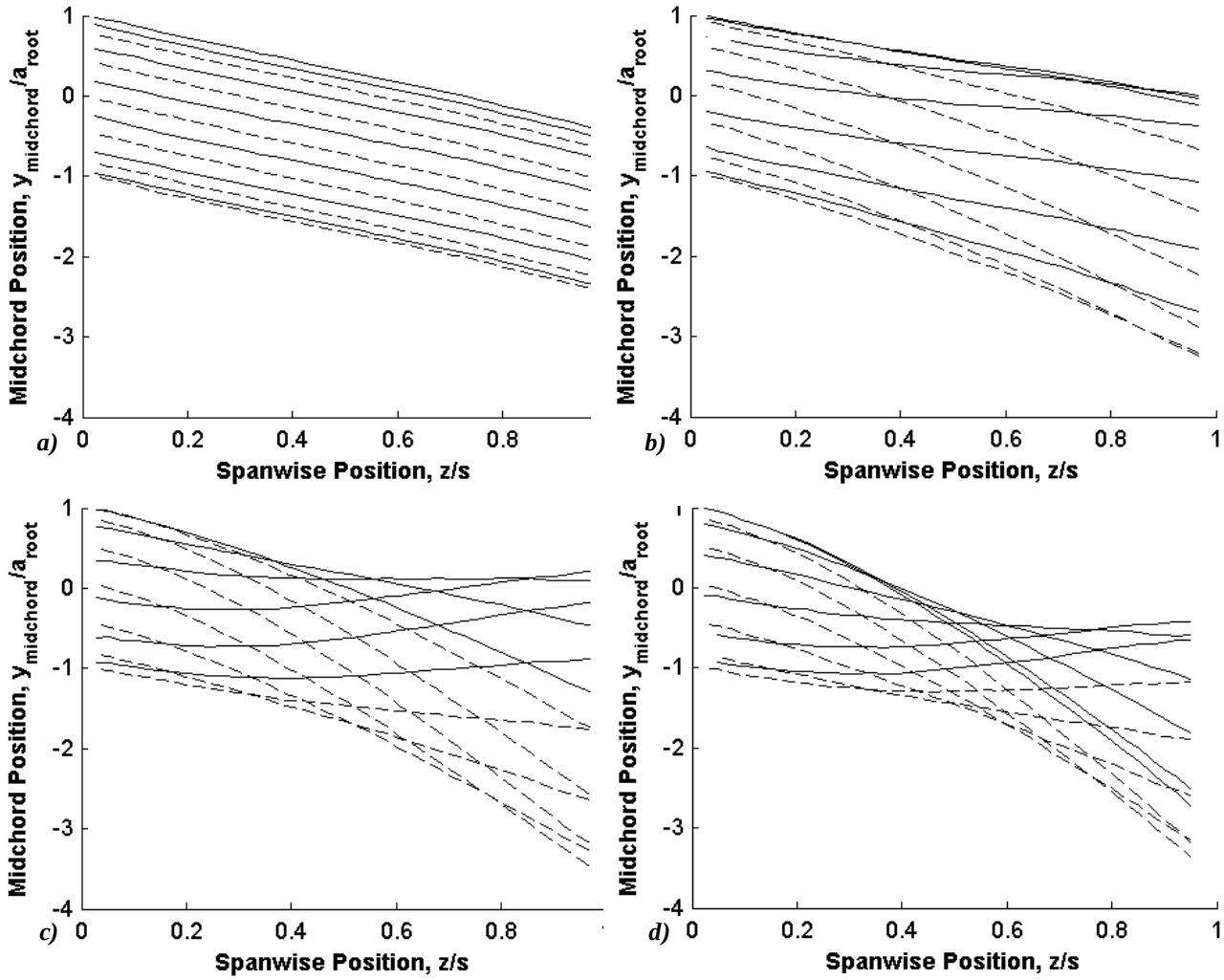

Fig. 10 Midchord position of the highly flexible wing normalized by the root amplitude for ten selected instants oscillating at: a) Sr_c = 0.075, b) Sr_c = 0.975, c) Sr_c = 1.500 and d) Sr_c = 2.025. Solid line is for the root moving downwards; dashed line is for the root moving upwards.

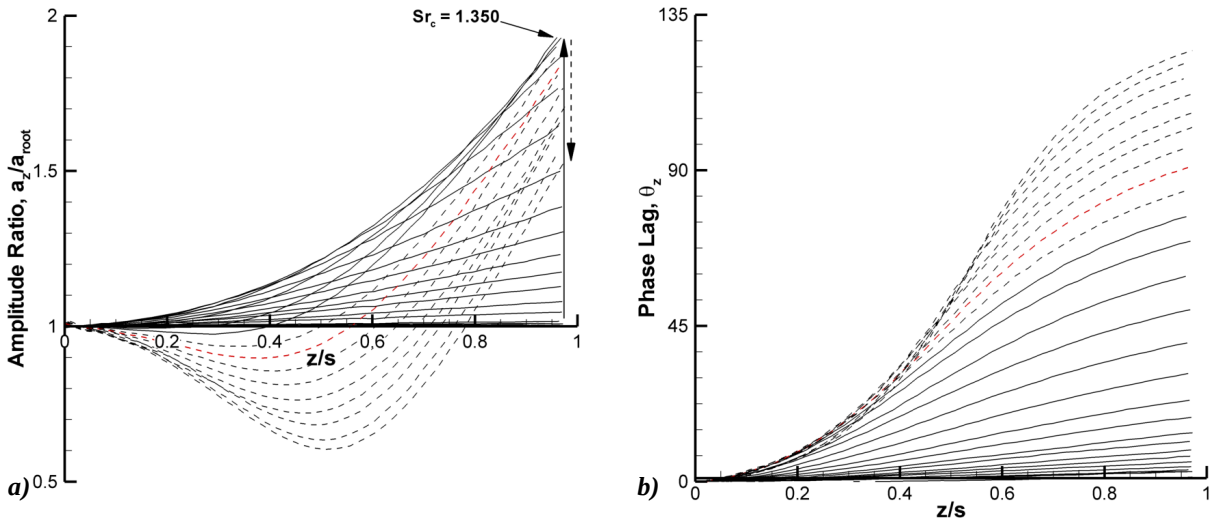

Fig. 11 a) Amplitude ratio and b) phase lag along the span of the highly flexible wing for Strouhal numbers in the range Sr_c = 0.075 : 0.075 : 2.025. Solid lines are Strouhal numbers below the peak tip amplitude ($Sr_c \leq$ 1.350); dashed lines are Strouhal numbers above the peak tip amplitude (Sr_c > 1.350). The red dashed line is Sr_c = 1.500 (natural frequency).

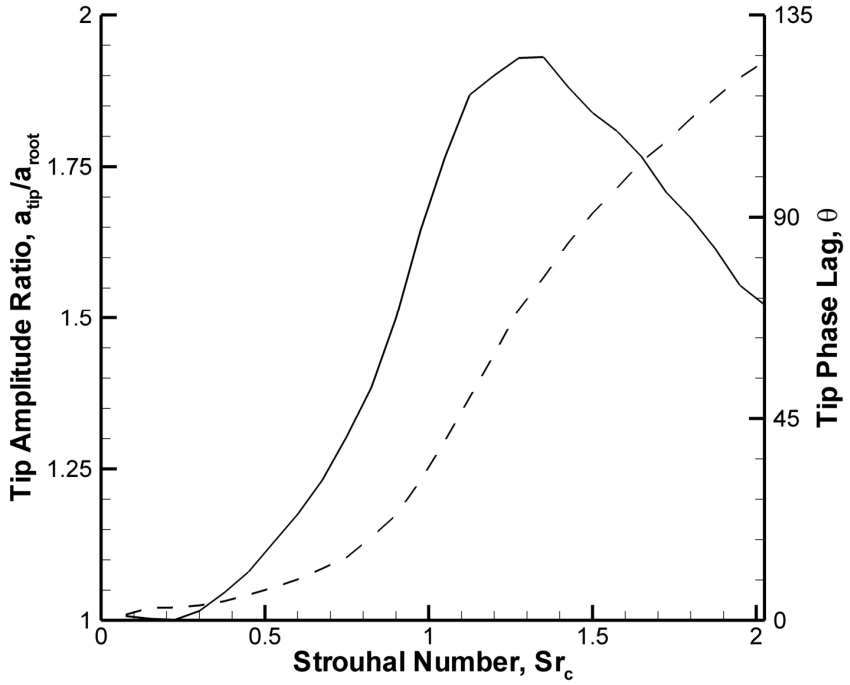

Fig. 12 Tip amplitude ratio (solid line) and tip phase lag (dashed line) against Strouhal number.

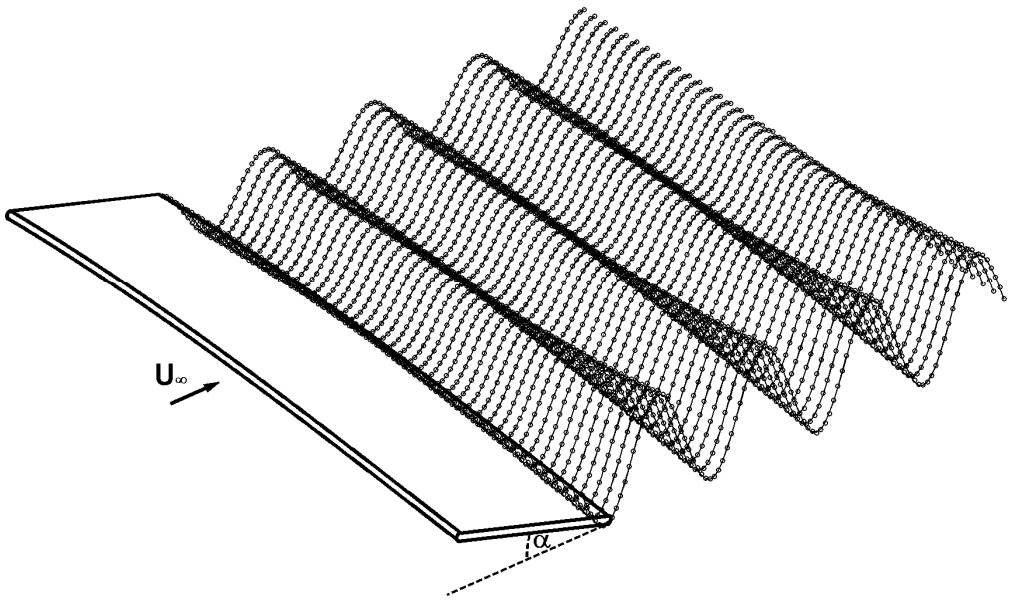

Fig. 13 Three dimensional representation of the deformation of the trailing-edge for the highly flexible wing oscillating with Sr_c = 1.500.

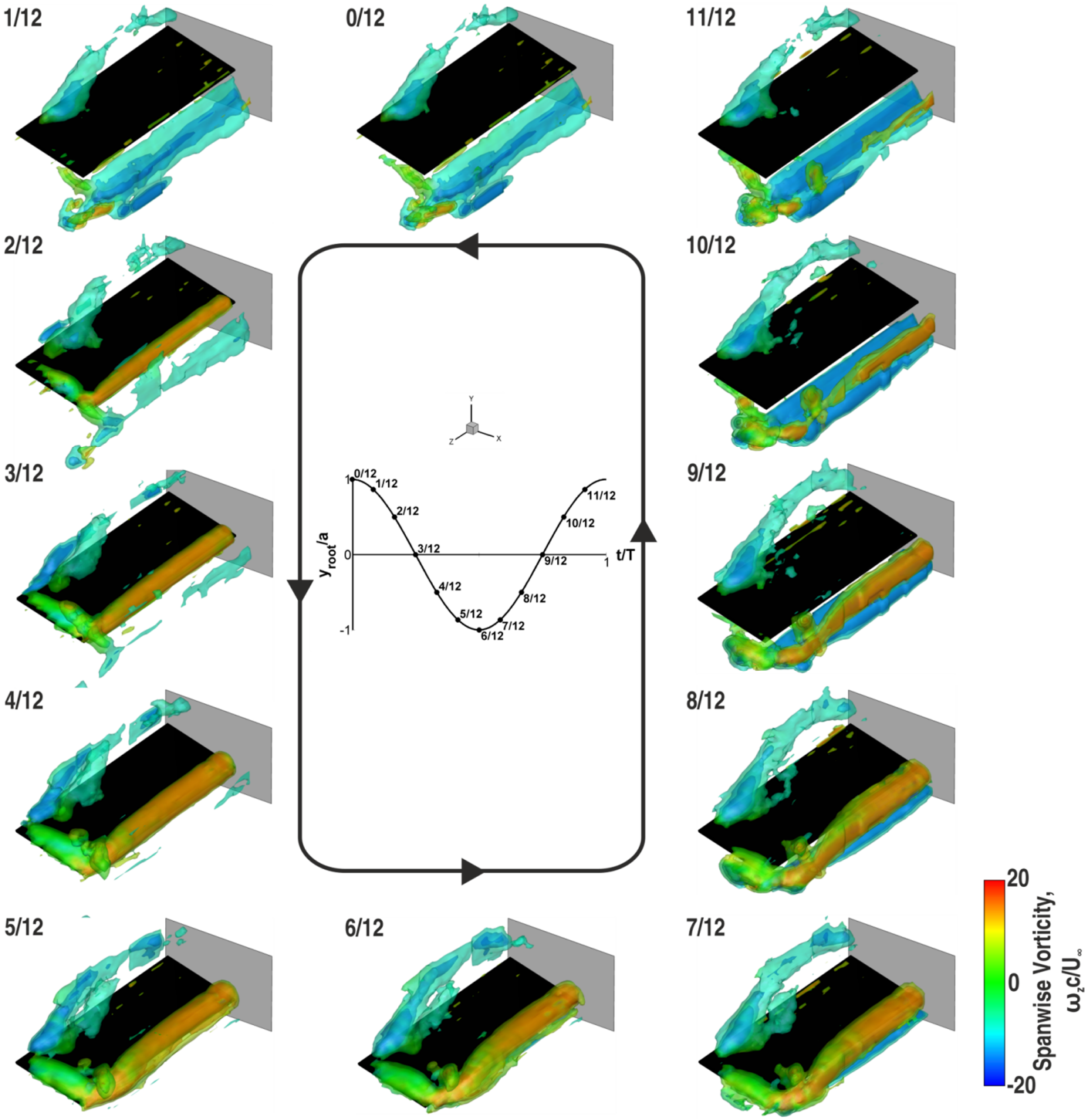

Fig. 14 Isosurfaces of phase-averaged vorticity magnitude ($\omega c/U_\infty$ = 8, 16, and 24) overlaid with spanwise vorticity for the rigid wing oscillating with Sr_c = 1.500.

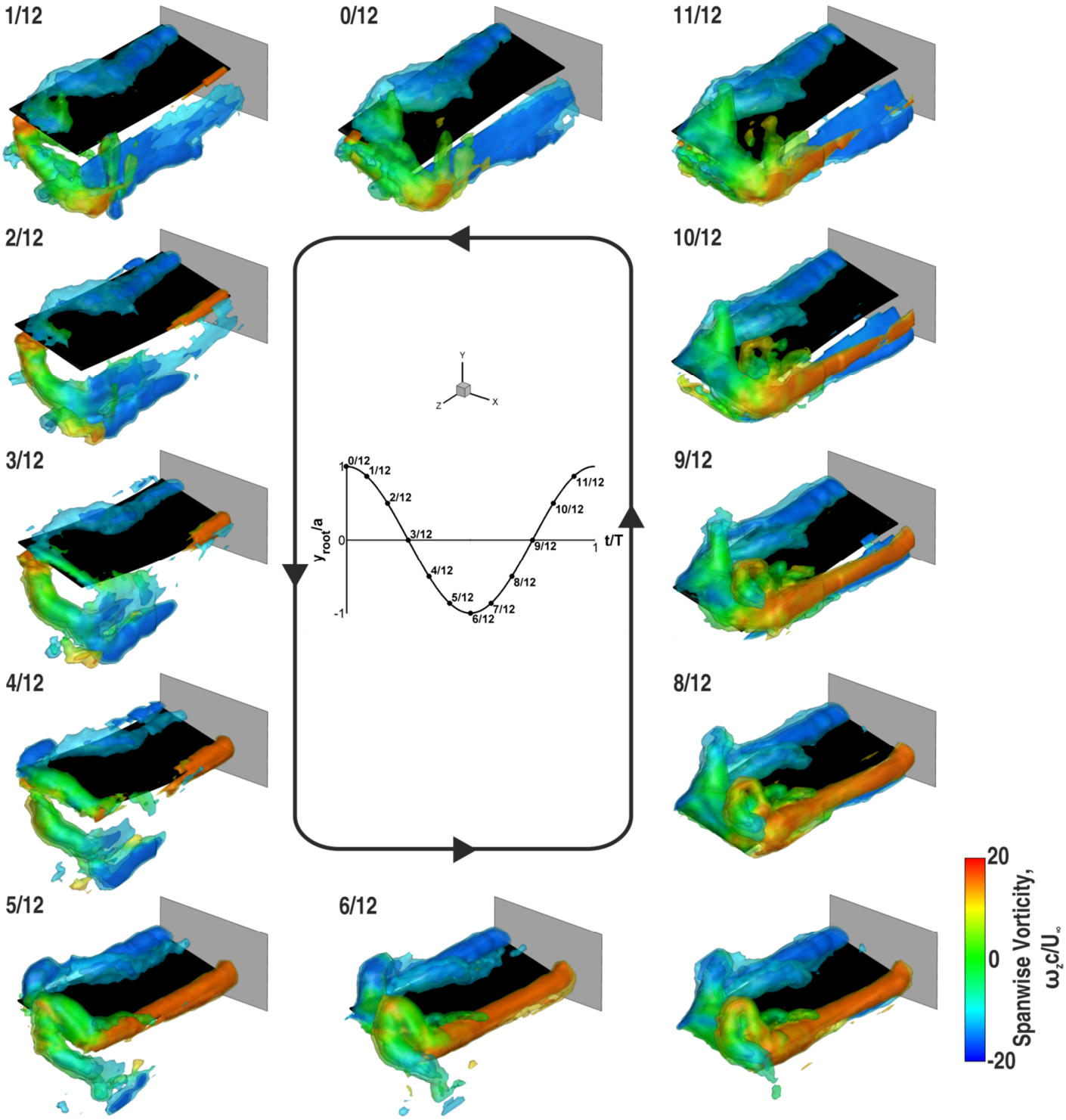

Fig. 15 Isosurfaces of phase-averaged vorticity magnitude ($\omega c/U_\infty$ = 12, 18, and 24) overlaid with spanwise vorticity for the highly flexible wing oscillating with Sr_c = 1.500.